University of Rhode Island

DigitalCommons@URI

Mechanical, Industrial & Systems Engineering Faculty Publications

Mechanical, Industrial & Systems Engineering

3-25-2020

Toward a unified interpretation of the “proper”/“smooth” orthogonal decompositions and “state variable”/“dynamic mode” decompositions with application to fluid dynamics

Arham Amin Khan

Joseph Kuehl

David Chelidze

Follow this and additional works at: https://digitalcommons.uri.edu/mcise_facpubs

AIP Advances

Toward a unified interpretation of the "proper"/"smooth" orthogonal decompositions and "state variable"/"dynamic mode" decompositions with application to fluid dynamics

Cite as: AIP Advances **10**, 035225 (2020); https://doi.org/10.1063/1.5144429
Submitted: 02 January 2020 . Accepted: 06 March 2020 . Published Online: 25 March 2020

Arham Amin Khan, Joseph Kuehl, and David Chelidze

View Online Export Citation CrossMark

ARTICLES YOU MAY BE INTERESTED IN

A two-dimensional transient fluid-thermal coupling method for temperature rising calculation of transformer winding based on finite element method
AIP Advances **10**, 035325 (2020); https://doi.org/10.1063/1.5141130

Multiphase flow mobility impact on oil reservoir recovery: An open-source simulation
AIP Advances **10**, 035032 (2020); https://doi.org/10.1063/5.0002719

Temperature expansions in the square-shoulder fluid. II. Thermodynamics
The Journal of Chemical Physics **152**, 124113 (2020); https://doi.org/10.1063/1.5142662

NEW
AVS Quantum Science
A new interdisciplinary home for impactful quantum science research and reviews
NOW ONLINE
Co-Published by AIP Publishing AVS

AIP Publishing

© 2020 Author(s).

Toward a unified interpretation of the "proper"/"smooth" orthogonal decompositions and "state variable"/"dynamic mode" decompositions with application to fluid dynamics

Cite as: AIP Advances 10, 035225 (2020); doi: 10.1063/1.5144429
Submitted: 2 January 2020 • Accepted: 6 March 2020 •
Published Online: 25 March 2020

View Online Export Citation CrossMark

Arham Amin Khan,[1,a] Joseph Kuehl,[1,b] and David Chelidze[2,c]

AFFILIATIONS

[1] Mechanical Engineering, University of Delaware, Newark, Delaware 19716, USA
[2] Mechanical, Industrial and Systems Engineering, University of Rhode Island, Kingston, Rhode Island 02881, USA

[a] Electronic mail: arham@udel.edu
[b] Author to whom correspondence should be addressed: jkuehl@udel.edu
[c] Electronic mail: chelidze@uri.edu

ABSTRACT

A common interpretation is presented for four powerful modal decomposition techniques: "proper orthogonal decomposition," "smooth orthogonal decomposition," "state-variable decomposition," and "dynamic mode decomposition." It is shown that, in certain cases, each technique can be interpreted as an optimization problem and similarities between methods are highlighted. By interpreting each technique as an optimization problem, significant insight is gained toward the physical properties of the identified modes. This insight is strengthened by being consistent with cross-multiple decomposition techniques. To illustrate this, an inter-method comparison of synthetic hypersonic boundary layer stability data is presented.

© 2020 Author(s). All article content, except where otherwise noted, is licensed under a Creative Commons Attribution (CC BY) license (http://creativecommons.org/licenses/by/4.0/). https://doi.org/10.1063/1.5144429

I. INTRODUCTION

Modal decomposition techniques are powerful tools for the investigation of the dynamics underlying various systems. These decomposition techniques tend to fall into one of the two categories: (a) techniques that optimally account for data variance, i.e., reproduce the dataset with a minimal number of modes, and (b) techniques that seek to identify dynamically relevant (or physical) modes without requiring extensive knowledge of the system. As most modal decomposition techniques are statistical in nature, caution must be practiced when attempting the latter. In such cases, additional constraints are applied to the statistical methods in an effort to isolate the physically relevant aspects of the data. In the end, the user must interpret the identified modes based on the statistical method used, data preprocessing performed, and constraints applied.

When performing a modal analysis, it is of great importance to have a fundamental understanding of the chosen method and ideally, this understanding should be consistent across a number of available methods to build intuition. This manuscript provides a common interpretation of four popular (and powerful) modal decomposition techniques; the so-called "Proper Orthogonal Decomposition" (POD[1,2]), "Smooth Orthogonal Decomposition" (SOD[3]), "State-Variable Decomposition" (S-VD[4,5]), and "Dynamic Mode Decomposition" (DMD[6]), thereby allowing for improved mode interpretation and cross-method comparison.

Note that the treatments of POD, SOD, and S-VD given below are relatively standard and can be found in several other references.

© Author(s) 2020

Here, the works of Chelidze and co-workers[3,7–10] and the recent work of Kuehl[11] are followed. There are also many treatments of DMD available in the literature, which usually focus on the Krylov subspace interpretation. Here, the focus will be on several works of Schmid and co-workers[6,12,13] and Kutz.[14] The main contribution of the present work is a unified (though only for restricted cases) interpretation of POD, SOD, S-VD, and DMD, in which each method can be interpreted as a constrained maximization problem.

II. BACKGROUND

In what follows, we consider the decomposition of a data matrix $X = [x_1, x_2, \ldots, x_n]^T \in \mathbb{R}^{n\times m}$, which contains multivariate time series of measurements $\{x_i \in \mathbb{R}^{m\times 1}\}_{i=1}^{n}$ taken at m different spatial locations at n time instants. It is usually assumed that each column of X has zero mean. Alternatively, we make each column of X zero-mean as part of preprocessing. In particular, we are looking for separation into temporal coordinates and spatial modes,

$$X = \sum_{k=1}^{m} q_k \phi_k^T = Q\Phi^T, \tag{1}$$

where $\phi_k \in \mathbb{R}^{m\times 1}$ represent spatial modes that are columns of matrix $\Phi \in \mathbb{R}^{m\times m}$ and $q_k \in \mathbb{R}^{n\times 1}$ represent the corresponding temporal coordinates that constitute the columns of matrix $Q \in \mathbb{R}^{n\times m}$.

If the spatial modes are orthonormal, then one can obtain the time coordinates as follows:

$$Q = X\Phi \quad \text{or} \quad q_i = X\phi_i. \tag{2}$$

On the other hand, if they are just linearly independent unit vectors, which are not orthogonal, denoting adjoint modes $\Psi = \Phi^{-T}$ yields

$$Q = X\Phi^{-T} = X\Psi \quad \Rightarrow \quad q_i = X\psi_i. \tag{3}$$

Therefore, ψ_i and ϕ_i are biorthonormal (i.e., $\Psi^T\Phi = I$, or $\psi_i^T\phi_j = \delta_{ij}$), and we can write $X = X\Psi\Phi^T$.

A. Proper orthogonal decomposition

Let us begin with the POD technique, which is also known as "Empirical Orthogonal Functions" (EOFs), "Principle Component Analysis" (PCA), and "Karhunen–Loève Decomposition" depending on the field of study. Despite the differences in the name, almost all implementations of the method are the same. A Singular Value Decomposition (SVD) is performed on the data matrix X, which decomposes the data into statistical *normal* modes, which optimally account for the data's amplitude variance and also allows for a convenient geometric interpretation. When considering a cloud of particles in a D dimensional space, the SVD of this cloud yields a set of D singular values and singular vectors. The singular values reflect the length of the semi-axes of an ellipsoid encompassing the cloud of particles, with the corresponding directions given by the singular vectors. While this interpretation is insightful, the essence of the technique is most transparent when formulated as a constrained maximization problem. POD fundamentally considers those modes, which maximize the amplitude variance of the projection,

$$\max_{\phi} \|X\phi\|^2 \quad \text{with} \quad \phi^T\phi = 1, \tag{4}$$

or the corresponding Rayleigh's quotient

$$\max_{\phi}\left\{\lambda(\phi) = \frac{\|X\phi\|^2}{\|\phi\|^2}\right\} \Rightarrow \max_{\phi}\left\{\lambda'(\phi) = \frac{\phi^T\Sigma_{xx}\phi}{\phi^T\phi}\right\}, \tag{5}$$

where Σ_{xx} is the covariance matrix of X, $\phi \in \mathbb{R}^{m\times 1}$, and $\lambda = (n-1)\lambda'$. Variational techniques may be applied to obtain the eigenvalue problem $\Sigma_{xx}\phi_i = \lambda_i\phi_i$, or correspondingly, the SVD expression of $X = UC\Phi^T$. Note that the columns of unitary matrix Φ are eigenvectors of Σ_{xx}, and $Q = UC$, where U and C are unitary and rectangular diagonal matrixes, respectively. From this formulation, it is clear that POD is an amplitude based projection, which results in a sequence of orthonormal modes, ϕ_i, that optimally account for the amplitude variance of X in the corresponding q_is.

B. Smooth orthogonal decomposition

The idea of SOD was first explored by Chatterjee *et al.*[15] and later formalized by Chelidze and Zhou[3] in the context of nonlinear vibrations, who provided a thorough treatment, including computational details and its many beneficial properties.[7–10] Again, the current work will simply highlight key aspects of the method. SOD considers the constrained maximization problem

$$\max_{\psi_s}\|X\psi_s\|^2 \quad \text{subject to} \quad \min_{\psi_s}\|V\psi_s\|^2, \tag{6}$$

where V is the temporal derivative of X. The corresponding generalized Rayleigh's quotient is

$$\max_{\psi_s}\left\{\lambda_s = \frac{\|X\psi_s\|^2}{\|V\psi_s\|^2}\right\} \Rightarrow \max_{\psi_s}\left\{\lambda_s = \frac{\psi_s^T\Sigma_{xx}\psi_s}{\psi_s^T\Sigma_{vv}\psi_s}\right\}, \tag{7}$$

where Σ_{vv} is the covariance matrix of V and λ_s are the smoothed orthogonal values (SOVs). Variational techniques may again be applied and result in the generalized eigenvalue problem $\Sigma_{xx}\psi_{s,i} = \lambda_{s,i}\Sigma_{vv}\psi_{s,i}$ or correspondingly a generalized singular value decomposition (GSVD) problem for $X = U_sC_s\Phi_s^T$ and $V = W_sS_s\Phi_s^T$. Generalized singular vectors and eigenvectors are related by $\Psi_s^{-1} = \Phi_s^T$, where $\Psi_s = [\psi_{s,1}, \psi_{s,2}, \ldots, \psi_{s,m}]$ and $X\Psi_s = Q_s$. It follows that SOD considers those modes that maximize amplitude variance of projection, while at the same time being as smooth in time as possible. As nature tends to behave in a "smooth" fashion, this "smoothness" property has been shown to be more physically relevant than the amplitude only based POD analysis.[8]

It should be noted that POD, by definition, identifies orthogonal modes, while SOD results in non-orthogonal modes. This is of particular importance to non-self-adjoint problems in which the physical mechanisms that govern the system dynamics are not orthogonal. The columns of matrix $Q_s = U_sC_s$ contain time coordinates of the corresponding modes in Φ_s, and since U_s is unitary and C_s is diagonal, time coordinates remain *orthogonal*. This probably motivates the use of "orthogonal" in the name SOD. Hence, SOD has *only temporal orthogonality* ($u_{s,i}^T u_{s,j} = \delta_{ij}$), while POD has both temporal and spatial orthogonality ($u_i^T u_j = \phi_i^T\phi_j = \delta_{ij}$).

While $\Psi_s = \Phi_s^{-T}$, we can also determine eigenvectors without taking an inverse of singular vectors as $\Psi_s = (X^TX)^{-1}\Phi_sC_s^2 = (n-1)\Sigma_{xx}^{-1}\Phi_sC_s^2$. That is, the SOD technique immediately gives

© Author(s) 2020

both direction (Φ_s) and projection (Ψ_s) eigenvectors satisfying the biorthonormal condition. While this is a straightforward result, due to the lack of physical interpretation, this property has not been exploited. In particular, this allows for experimental "receptivity" studies for the investigation of how arbitrary disturbances excite non-orthogonal modes of oscillation in a system.

C. Dynamic mode decomposition

Recently, the "Dynamic Mode Decomposition" technique, developed by Schmid,[6] has been popularized. The work of Schmid[13] will provide a starting point of our treatment. The DMD method considers the mapping of data snapshot $X_1 = [x_1, x_2, \ldots, x_n]$ to $X_2 = [x_2, x_3, \ldots, x_{n+1}]$, where $X_1 = X^T \in \mathbb{R}^{m\times n}$ as used in SOD/POD and X_2 is one time sample delayed version of X_1 (there are also generalizations for the time-delay greater than one sample). In the case of $n > m$, it considers the following mapping:

$$X_2 = AX_1 + re^T, \tag{8}$$

where $A \in \mathbb{R}^{m\times m}$, $r \in \mathbb{R}^{m\times 1}$ is the vector of residuals, and $e \in \mathbb{R}^n$ is a zero vector except the last term $e_n = 1$. Then, A is chosen such that it minimizes the residual vector's norm in the least squares sense, $A = X_2X_1^T(X_1X_1^T)^{-1}$, and the DMD modes come from the eigen-decomposition of A. Alternatively, using QR decomposition of $X_1^T = Q_1R_1$, we get $A = X_2Q_1R_1^{-T}$. Note that since A may not be symmetric, we expect complex eigen-decompositions of A.

When $n < m$, as is frequently a case in flow data, or when rank of X_1 is smaller than m, the matrix A cannot be determined uniquely since $X_1X_1^T$ is rank deficient. Then, A is chosen such that each of the snapshots in X_2, $\{x_i\}_{i=2}^{n+1}$, can be written as a linear combination of snapshots in X_1, $\{x_i\}_{i=1}^{n}$. Since most of the snapshots in both datasets are the same except for the first and last snapshots in X_1 and X_2, respectively, Eq. (8) is rewritten as

$$X_2 = X_1S + re^T, \tag{9}$$

where $S \in \mathbb{R}^{n\times n}$ is the companion matrix of A,

$$S = \begin{pmatrix} 0 & 0 & \cdots & 0 & a_1 \\ 1 & 0 & \cdots & 0 & a_2 \\ 0 & 1 & \cdots & 0 & a_3 \\ \vdots & \vdots & \ddots & \vdots & \vdots \\ 0 & 0 & \cdots & 1 & a_n \end{pmatrix}. \tag{10}$$

Using the QR decomposition of $X_1 = Q_1R_1$, we find $a = R_1^{-1}Q_1^Tx_{n+1}$. Now, if $y_{d,i}$ is an eigenvector of S then $X_1y_{d,i} \cong \phi_{d,i}$ is an approximation of an eigenvector of A, and eigenvalues of S are the approximations of eigenvalues of A.

Alternatively, we can assume X_2 to be a linear combination of columns in Φ from the SVD of $X_1 = X^T = \Phi CU^T$. Then, one can determine a similarity transform of A as $\tilde{S} = \Phi^TA\Phi = \Phi^TX_2UC^{-1}$. Consequently, the eigenvalues of A are approximated by the eigenvalues of $\tilde{S}$, $\lambda_{d,i}$, and the corresponding eigenvectors are given by $\Phi\,\tilde{y}_{d,i} \cong \phi_{d,i}$, where $\tilde{y}_{d,i}$ are the eigenvectors of $\tilde{S}$.

D. State-variable decomposition

Shortly after SOD, and recognizing that it cannot provide complex modes, S-VD was proposed to identify complex vibration modes and the associated damping ratios and frequencies of the state-variable model of a multi-degree-of-freedom linear system.[5] In this approach, S-VD is accomplished by solving an asymmetric generalized eigenvalue problem,

$$\Sigma_{xv}\psi_v = \lambda_v\Sigma_{xx}\psi_v, \tag{11}$$

where Σ_{xx} is a covariance matrix of a free-vibration time series of state-variables in X, and Σ_{xv} is the corresponding cross-covariance matrix between X and its time derivative V. Then, the complex vibration modes are approximated by the columns of $\Phi_v^T = \Psi_v^{-1}$ and the corresponding eigenvalues λ_v approximate $-\zeta_j\omega_j \pm i\omega_j\sqrt{1-\zeta_j}$, where ζ_j and ω_j are the damping ratios and the natural frequencies of the jth mode.

When comparing SOD and S-VD as applied to the free-vibrations of a linear multi-degree-of-freedom system, both give the same modes for undamped or proportionally damped systems. For generally damped systems, the SOD results in the eigenvalues that come in closely spaced pairs, and we conjecture (and provide an explicit example later) that the corresponding pair of eigenvectors spans approximately the same planar subspace of the state space as the complex conjugate pairs of eigenvectors from the S-VD.

The S-VD can also be derived from these simple equations,

$$X = Q_v\Phi_v^T, \text{ and } V = \dot{X} = \dot{Q}_v\Phi_v^T = Q_v\Lambda_v\Phi_v^T, \tag{12}$$

where Λ is a companion matrix of temporal differential operator and it is a diagonal matrix since every column in Q_v is described by a single exponential response function $\exp\left[\left(-\zeta_j\omega_j \pm i\omega_j\sqrt{1-\zeta_j}\right)t\right]$. Now, remembering that $\Psi_v^{-1} = \Phi_v^T$, we get

$$X\Psi_v = Q_v \quad \text{and} \quad V\Psi_v = Q_v\Lambda_v. \tag{13}$$

Thus,

$$V\Psi_v = X\Psi_v\Lambda_v. \tag{14}$$

Now, if we multiply both sides from the left by $\Psi_v^*X^T$,

$$\Psi_v^*X^TV\Psi_v = \Psi_v^*X^TX\Psi_v\Lambda_v, \tag{15}$$

or we obtain the S-VD,

$$X^TV\Psi_v = X^TX\Psi_v\Lambda_v. \tag{16}$$

III. ALTERNATE INTERPRETATIONS

We have shown that the optimization interpretation is a physically insightful approach. In the following, we interpret limited cases of the DMD as an optimization problem.

A. DMD as an optimization

Fundamentally, DMD considers the adjoint eigenvalue problem of A, $\psi_d^*A = \lambda_d^*\psi_d^*$, for $n > m$, and the eigenvalue problem of

© Author(s) 2020

S, $Sy_d = \lambda_d y_d$ for $n < m$. Using relationship (8) and (9), these are equivalent to the generalized eigenvalue problems

$$\psi_d^* X_2 = \lambda_d^* \psi_d^* X_1 \quad \text{and} \quad X_2 y_d = \lambda_d X_1 y_d. \tag{17}$$

The former of Eq. (17), upon multiplication from the right by $X_1^T \psi_d$ or $X_2^T \psi_d$, or by taking its magnitude, yields

$$\begin{aligned} \psi_d^* X_2 X_1^T \psi_d &= \lambda_d^* \psi_d^* X_1 X_1^T \psi_d, \\ \psi_d^* X_2 X_2^T \psi_d &= \lambda_d^* \psi_d^* X_1 X_2^T \psi_d, \\ \psi_d^* X_2 X_2^T \psi_d &= (\lambda_d^* \lambda_d) \psi_d^* X_1 X_1^T \psi_d. \end{aligned} \tag{18}$$

Multiplying the first of Eq. (18) by λ_d and adding the second yields

$$\psi_d^* \left[\lambda_d^* X_1 X_2^T + \lambda_d X_2 X_1^T \right] \psi_d = (\lambda_d \lambda_d^*) \psi_d^* X_1 X_1^T \psi_d + \psi_d^* X_2 X_2^T \psi_d. \tag{19}$$

Utilizing the third of Eq. (18) leads to

$$\psi_d^* \left[\lambda_d^* X_1 X_2^T + \lambda_d X_2 X_1^T \right] \psi_d = 2 \psi_d^* X_2 X_2^T \psi_d. \tag{20}$$

For the general case of DMD, complex λ_d and ψ_d, we can proceed no further with the optimization analysis as was done for POD and SOD. However,

1. Case 1

For the case of purely exponentially growing disturbances (i.e., non-propagating, exponentially growing disturbances with purely real λ_d and ψ_d), Eq. (20) allows for the DMD to be formulated as

$$\lambda_{d(R)} = \frac{2 \psi_d^* X_2 X_2^T \psi_d}{\psi_d^* \left[X_1 X_2^T + X_2 X_1^T \right] \psi_d}. \tag{21}$$

Noting that the quantities $\left[X_1 X_2^T + X_2 X_1^T \right]$, $X_1 X_1^T$, and $X_2 X_2^T$ are all Hermitian, a Rayleigh quotient analysis may again be applied. In this case, it is found that the DMD satisfies the corresponding optimization problems

$$\max_{\psi_d} \| \sqrt{2} \; X_2^T \psi_d \|^2 \quad \text{subject to} \quad \min_{\psi_d} \| \sqrt{\left[X_1 X_2^T + X_2 X_1^T \right]}^T \psi_d \|^2. \tag{22}$$

It follows that for the special case of purely exponentially growing disturbances, the DMD seeks to identify those modes, which maximize their modal projection onto the time-shifted data matrix while minimizing their projection onto the covariance matrix of the data and time-shifted data.

2. Case 2

For the case of purely oscillatory, neutral disturbances (i.e., non-propagating nor exponentially growing disturbances with purely imaginary λ_d and real ψ_d), the DMD may be formulated by considering Eq. (17) and multiplying them by their complex conjugate transpose from the right and left, respectively, which yields

$$\psi_d^* X_2 X_2^T \psi_d = (\lambda_d^* \lambda_d) \psi_d^* X_1 X_1^T \psi_d \tag{23}$$

and

$$y_d^* X_2^T X_2 y_d = (\lambda_d^* \lambda_d) y_d^* X_1^T X_1 y_d, \tag{24}$$

or

$$|\lambda_d|^2 = \frac{\psi_d^* X_2 X_2^T \psi_d}{\psi_d^* X_1 X_1^T \psi_d} \quad \text{and} \quad |\lambda_d|^2 = \frac{y_d^* X_2^T X_2 y_d}{y_d^* X_1^T X_1 y_d}. \tag{25}$$

This "magnitude" DMD decomposition can be solved by the following generalized eigenvalue problems:

$$\Sigma_2 \psi_d = |\lambda_d|^2 \Sigma_1 \psi_d \quad \text{and} \quad \Gamma_2 y_d = |\lambda_d|^2 \Gamma_1 y_d, \tag{26}$$

where $\Sigma_i = X_i X_i^T / (n-1)$ and $\Gamma_i = X_i^T X_i / (m-1)$ are temporal and spatial covariance matrices of X_i, respectively. It is observed that the magnitude of the DMD can also be interpreted as the generalized eigenvalue problem (for $|\lambda_d|^2$) of the map-shifted data correlation matrix (Σ_2 or Γ_2) and the original data correlation matrix (Σ_1 or Γ_1). Furthermore, the magnitude of the DMD problem (for purely oscillatory, neutral disturbances) for $n > m$ can be formulated as the constrained maximization problem

$$\max_{\psi_d} \| X_2^T \psi_d \|^2 \quad \text{subject to} \quad \min_{\psi_d} \| X_1^T \psi_d \|^2, \tag{27}$$

or if $n < m$,

$$\max_{y_d} \| X_2 y_d \|^2 \quad \text{subject to} \quad \min_{y_d} \| X_1 y_d \|^2. \tag{28}$$

It follows that for the special case of purely oscillatory, neutral disturbances, the DMD seeks to identify those modes, which maximize their modal projection onto the time-shifted data matrix while minimizing their projection onto the original data matrix.

IV. CONNECTIONS BETWEEN METHODS

As stated in Introduction, when performing a modal analysis, it is of great importance to have a fundamental understanding of the chosen method and, ideally, this understanding should be consistent across a number of available methods to build intuition. Here, we outline connections between the methods considered in this manuscript.

A. Connecting SOD to S-VD

Considering the response of a multi-degree-of-freedom linear state-space model, SOD gives its real-valued decomposition

$$X = Q_s \Phi_s^T, \quad \text{and} \quad V = \dot{Q}_s \Phi_s^T = Q_s \Gamma_s \Phi_s^T, \tag{29}$$

where $\Gamma_s = \text{diag}(\gamma_{s,i})$ is a diagonal matrix. Since the columns of Q_s are orthogonal by definition, their time derivatives are also orthogonal to each other. Using $\Psi_s^{-1} = \Phi_s^T$, we can write

$$V \Psi_s = X \Psi_s \Gamma_s \;\Rightarrow\; V \psi_s = \gamma_s X \psi_s. \tag{30}$$

© Author(s) 2020

Now, multiplying both sides from the left by their transpose, we get

$$\psi_s^T V^T V \psi_s = \gamma_s^2 \psi_s^T X^T X \psi_s, \tag{31}$$

or using the generalized Rayleigh's quotient form,

$$\gamma_s(\psi_s)^2 = \frac{\psi_s^T \Sigma_{vv} \psi_s}{\psi_s^T \Sigma_{xx} \psi_s}, \tag{32}$$

which has the same stationary values as SOD if we let $\lambda_s = \gamma_s^{-2}$. It is clear that if the system has real vibration modes, then SOD and S-VD are directly related to $\Gamma_s = \Lambda_v = \Lambda_s^{-\frac{1}{2}}$.

However, when vibration modes are complex, we can use Eq. (29) to write

$$V\psi_v = \lambda_v X \psi_v, \tag{33}$$

and multiplying both sides by their complex conjugate transpose, we get

$$\psi_v^* V^T V \psi_v = \lambda_v \lambda_v^* \psi_v^* X^T X \psi_v, \tag{34}$$

or using the generalized Rayleigh's quotient form,

$$|\lambda_v(\psi_v)|^2 = \frac{\psi_v^* \Sigma_{vv} \psi_v}{\psi_v^* \Sigma_{xx} \psi_v}, \tag{35}$$

which now is a real-valued quotient and has its stationary values at

$$\gamma_s^2 = \lambda_s^{-1} = \min_{\psi_v} \frac{\psi_v^* \Sigma_{vv} \psi_v}{\psi_v^* \Sigma_{xx} \psi_v} = \min_{\psi_s} \frac{\psi_s^T \Sigma_{vv} \psi_s}{\psi_s^T \Sigma_{xx} \psi_s}. \tag{36}$$

We expect γ_s to be near the corresponding $|\lambda_v|$ and reflect the minimal ratio between the velocity and the displacement magnitudes.

B. Connecting S-VD to DMD

Again, considering the adjoint eigenvalue problem of A, $A^T \psi_d = \lambda_d \psi_d$, and denoting $X_2^T = X + V$, where V can be considered as the time derivative of X or change in the data matrix, we can rewrite Eq. (8) as

$$X + V = XA^T + er^T. \tag{37}$$

Dropping the residual, multiplying Eq. (37) by ψ_d, and using the adjoint eigen-decomposition of A, we get

$$(X + V)\psi_d = \lambda_d X \psi_d \quad \rightarrow \quad V\psi_d = (\lambda_d - 1) X \psi_d. \tag{38}$$

Multiplying the right expression of Eq. (38) from the left by $\psi_d^* V^T$ yields

$$\psi_d^* V^T V \psi_d = (\lambda_d - 1) \psi_d^* V^T X \psi_d \tag{39}$$

or

$$\Sigma_{vv} \psi_d = (\lambda_d - 1) \Sigma_{vx} \psi_d. \tag{40}$$

Therefore, S-VD's eigenvectors are related to the adjoint eigenvectors of the DMD matrix A, $\psi_d \cong \psi_v$, and the corresponding eigenvalues are related as $\lambda_d \cong \lambda_v + 1$. If $V = X_2 - X_1$, then S-VD and DMD modes are exactly the same.

C. Connecting SOD to "magnitude" DMD

Again, considering the adjoint eigenvalue problem of A, $A^T \psi_d = \lambda_d \psi_d$, and denoting $X_2^T = X + V$, where V can be considered as the time derivative of X or change in the data matrix, we can rewrite Eq. (8) as

$$X + V = XA^T + er^T. \tag{41}$$

Dropping the residual, multiplying Eq. (41) by ψ_d, and using the adjoint eigen-decomposition of A, we get

$$(X + V)\psi_d = \lambda_d X \psi_d \quad \rightarrow \quad V\psi_d = (\lambda_d - 1) X \psi_d. \tag{42}$$

Multiplication of the right expression of Eq. (42) by its complex conjugate transpose from the left yields

$$\psi_d^* V^T V \psi_d = |\lambda_d - 1|^2 \psi_d^* X^T X \psi_d \tag{43}$$

or re-writing it in a generalized Rayleigh's quotient form

$$|\lambda_d - 1|^2 = \frac{\psi_d^* \Sigma_{vv} \psi_d}{\psi_d^* \Sigma_{xx} \psi_d}. \tag{44}$$

Applying variational techniques to Eq. (44), we get $\Sigma_{vv} \psi_d = |\lambda_d - 1|^2 \Sigma_{xx} \psi_d$. Therefore, SOD's eigenvectors are related to the adjoint eigenvectors of the DMD matrix A, $\psi_d \cong \psi_s$, in the "magnitude" interpretation. The generalized Rayleigh's quotients for SOD [Eq. (7)] and magnitude-type DMD [Eq. (44)] are the inverse of each other. Thus, SOD solves an adjoint magnitude DMD problem for $n > m$ as the constrained maximization problem

$$\max_{\psi_d} \|(X_2^T - X_1^T)\psi_d\|^2 \quad \text{subject to} \quad \min_{\psi_d} \|X_1^T \psi_d\|^2, \tag{45}$$

or if $n < m$,

$$\max_{y_d} \|(X_2 - X_1) y_d\|^2 \quad \text{subject to} \quad \min_{y_d} \|X_1 y_d\|^2. \tag{46}$$

In fact the GSVD solution to SOD is the same as the magnitude of DMD if one considers the velocity matrix as $V = X_2^T - X_1^T$ (forward difference approximation for velocity). Equations (45) and (46) show that DMD's left- and right-hand eigenvectors approximate SOD eigenvectors $\psi_s \cong \psi_d$ and $\phi_s \cong \phi_d$, respectively, and the corresponding eigenvalues $\lambda_s \cong |\lambda_d - 1|^{-2}$.

It is clear from this interpretation that magnitude DMD identifies modes associated with the varying component of the data. Equations (45) and (46) show that DMD considers those modes that maximize projection onto the variable part of the flow while minimizing projection onto the flow field itself. This, of course, is consistent with Eqs. (27) and (28) in which modes are found that maximize amplitude variance projection on the map-shifted data while minimizing amplitude variance projection on the original data.

© Author(s) 2020

V. EXAMPLE: SYNTHETIC DATA OF HYPERSONIC BOUNDARY LAYER INSTABILITY

To illustrate the above modal decomposition properties, we now consider a synthetic dataset relevant to hypersonic boundary layer instability. Note that numerous variants of each decomposition technique exist in the literature (especially POD); however, here, we choose to focus on the fundamental nature of each method, as described above. Flow over a flared cone at Mach 6 (Fig. 1, specifically at the Mach 6 Purdue Quiet Tunnel conditions) is known to exhibit laminar flow breakdown that is dominated by Mack's second-mode instability.[16,17] Second modes are thought to be trapped acoustic waves, which resonate within a thermoacoustic impedance well formed between the vehicle wall and the maximum boundary layer density gradient, with thermoacoustic Reynolds stresses providing the fundamental energy source.[18–20] As second-mode waves behave as wave packets (finite-frequency-bandwidth disturbances) in the boundary layer,[21–23] they exhibit a nonlinear breakdown physics that is particularly relevant to our investigation: (1) The primary 300 kHz second-mode wave packet grows linearly. (2) As the primary wave packet amplitude grows, the onset of nonlinearity is indicated by the growth of a 600 kHz wave packet first harmonic. (3) As the first harmonic grows, higher harmonics are generated, and a feedback onto the primary wave packet from the first harmonic generates spectral broadening, which leads to the generation of a low-frequency wave packet disturbance in the boundary layer.[24,25] Thus, at different stages of nonlinear breakdown, three (or more) distinctly separated frequency disturbances are present with either distinct amplitude separation (during early stages of nonlinear development) or similar amplitudes (during late stages of nonlinear breakdown). This is illustrated in Fig. 2, which shows Nonlinear Parabolized Stability Equation (NPSE) boundary layer stability calculations on a Mach 6 flared cone under Purdue Quiet Tunnel conditions.

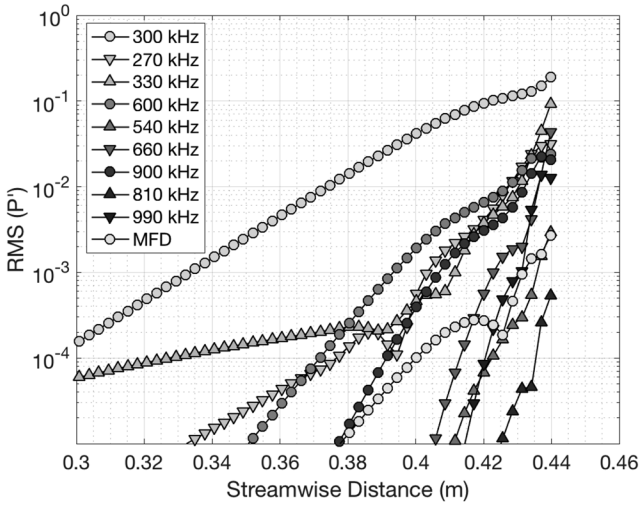

FIG. 2. NPSE root-mean-square of the disturbance amplitude vs the streamwise distance. Note: 300 kHz, 270 kHz, and 330 kHz—primary disturbance and its side lobes, respectively; 600 kHz, 540 kHz, and 660 kHz—first harmonic and side lobe harmonics, respectively; 900 kHz, 810 kHz, and 990 kHz—second harmonic and side lobe second harmonics, respectively; and MFD—mean flow distortion.

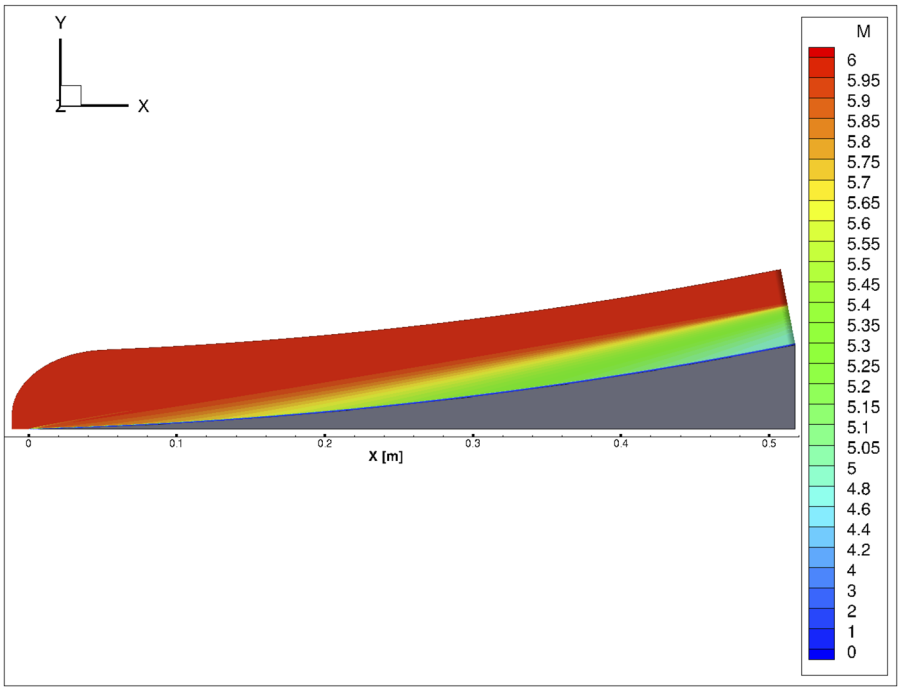

FIG. 1. Mach contours of a Mach 6 Purdue flared cone.

© Author(s) 2020

As the purpose of this manuscript is the investigation of modal decomposition and the example test case described above is simply to motivate our choice of synthetic data, we do not provide a detailed description of the calculations. For details of the numerical calculations (grid, flow parameters, etc.), identical to those used here, the interested reader is referred to Refs. 17 and 24. In general, basic state flow fields were calculated using US3D (a premiere hypersonic flow solver[26–28]) and stability calculations of this basic flow state were conducted with the JoKHeR NPSE solver.[23,29] The NPSE output provides wall-normal profiles of the complex disturbance shape functions, $\phi(y) = \phi_r(y) + i\phi_i(y)$, frequencies of each disturbance, and amplitudes of the disturbances along the length of the cone. From this output, we construct our synthetic dataset as follows:

Case 1: Pure Oscillation → Real(ϕ), Imaginary(ω),

$$\phi_T(y) = \sum_{j=1}^{3} A_j \phi_r^j(y) e^{\omega_j t} \quad \text{for} \quad t = [0, T], \tag{47}$$

where T is the observation time, $\phi_r^1(y)$ corresponds to the 300 kHz second-mode, $\phi_r^2(y)$ represents harmonics, $\phi_r^3(y)$ corresponds to the 30 kHz low-frequency disturbance, and A_j corresponds to the disturbance amplitude. Data will be generated for $A_1 > A_2 > A_3$, corresponding to the early stage nonlinearity, and

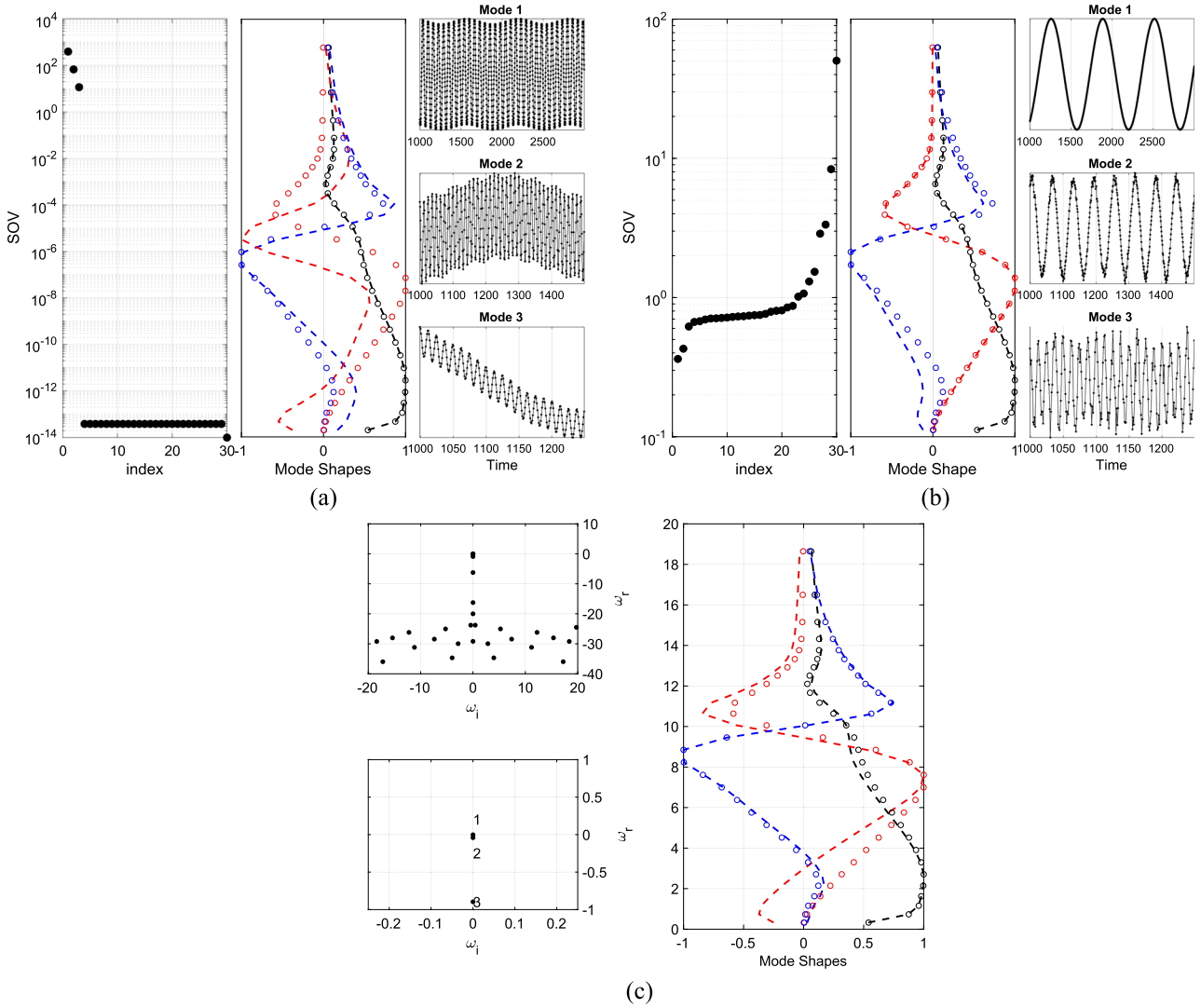

FIG. 3. Pure oscillations of the variable amplitude. POD (a) and SOD (b): spectra (left), mode shapes (middle), and amplitude coefficients (right). DMD (c): spectra (left) and mode shapes (right). Synthetic data input mode shapes are shown with open circles and decomposition mode shapes are shown with dashed lines. Mode shape are plotted against the y-axis nondimensionalized by the boundary layer length scale.

© Author(s) 2020

$A_1 \approx A_2 \approx A_3$, corresponding to the late stage nonlinear breakdown. In this case, disturbance shape functions are allowed to purely oscillate only.

Case 2: Propagating Oscillation → Complex(ϕ), Imaginary(ω),

$$\phi_T(y) = \sum_{j=1}^{3} A_j\left(\phi_r^j(y) + i\phi_i^j(y)\right)e^{\omega_j t} \quad \text{for} \quad t = [0, T]. \tag{48}$$

Again, data will be generated for $A_1 > A_2 > A_3$, corresponding to the early stage nonlinearity and $A_1 \approx A_2 \approx A_3$, corresponding to the late stage nonlinear breakdown. In this case, disturbance shape functions will be allowed to oscillate with phase propagation in the y-direction.

Case 3: General → Complex(ϕ), Complex(ω),

$$\phi_T(y) = \sum_{j=1}^{3} A_j\left(\phi_r^j(y) + i\phi_i^j(y)\right)e^{\omega_j t} \quad \text{for} \quad t = [0, T]. \tag{49}$$

Again, data will be generated for $A_1 > A_2 > A_3$, corresponding to the early stage nonlinearity and $A_1 \approx A_2 \approx A_3$, corresponding to the late stage nonlinear breakdown. In this case, disturbance shape functions will be allowed to oscillate with phase propagation in the y-direction and experience exponential growth in time.

For test cases with different amplitude disturbances, $A_2 = 1$, $A_1 = 3A_2$, and $A_3 = 0.33A_2$ are chosen. The disturbance frequencies are set to $\omega_1 = 0.1$, which represents the primary mode instability, $\omega_2 = 0.5$, which represents the harmonics, and $\omega_3 = 0.01$,

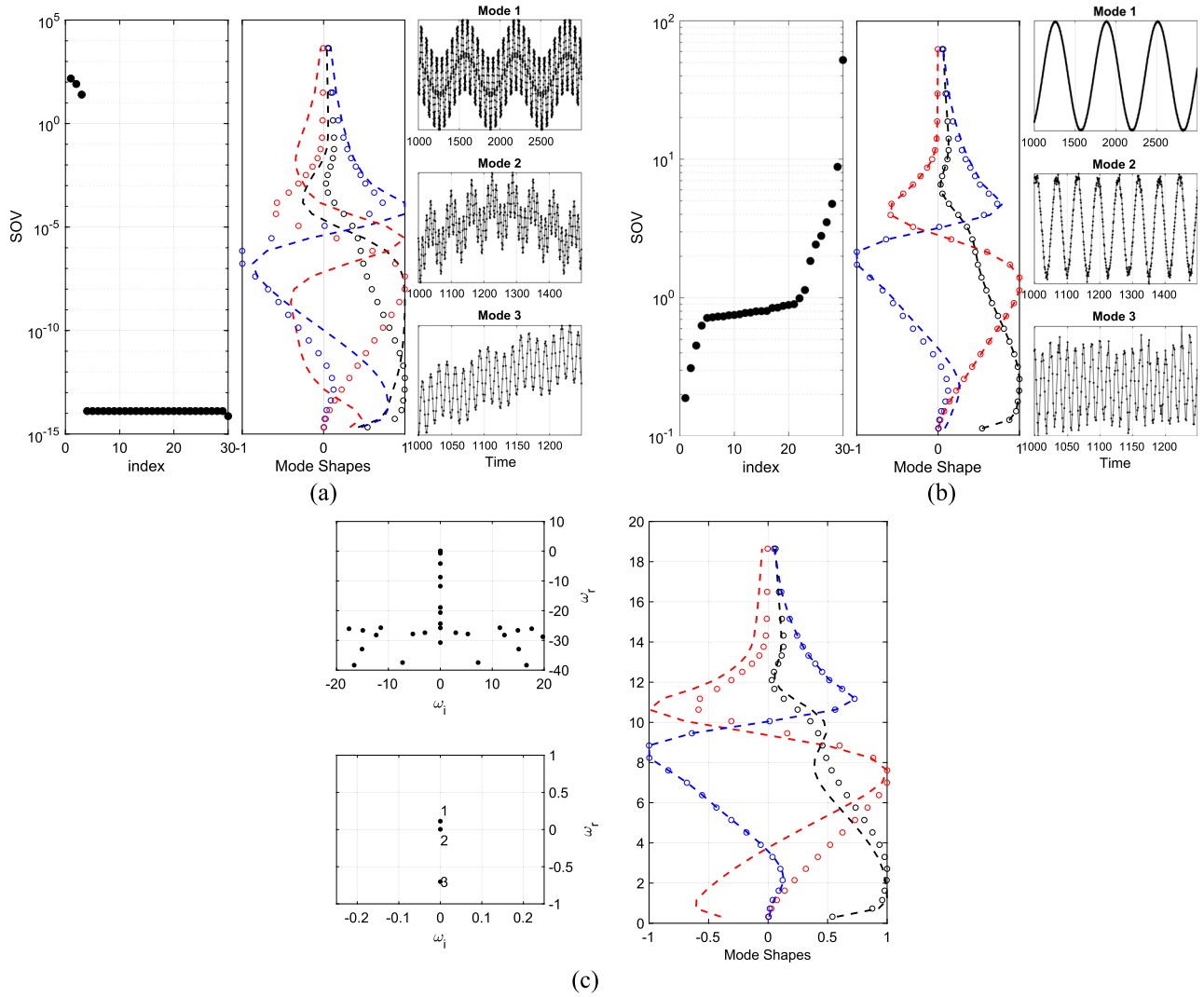

FIG. 4. Pure oscillations of the constant amplitude. POD (a) and SOD (b): spectra (left), mode shapes (middle), and amplitude coefficients (right). DMD (c): spectra (left) and mode shapes (right). Synthetic data input mode shapes are shown with open circles and decomposition mode shapes are shown with dashed lines. Mode shapes are plotted against the y-axis nondimensionalized by the boundary layer length scale.

© Author(s) 2020

which represents the low-frequency content. For the cases with exponential growth, growth rates are set to $\omega_1 = 3/T$, $\omega_2 = 2/T$, and $\omega_3 = 1/T$.

A. Test case results

1. Pure Oscillation: Real(ϕ), Imaginary(λ)

Modal decomposition of the "pure oscillation" synthetic dataset can be seen in Fig. 3, for the variable amplitude disturbance case, and in Fig. 4, for the constant amplitude disturbance case. As expected, all three decomposition techniques capture the modal structure fairly well. Notice that POD has identified that there are three dominant modes contributing to the signal, but slight contamination between the specific disturbance profiles is clear from consideration of the amplitude coefficients. SOD removes this contamination via its ability to partition signal variance based on both the amplitude and the time scale of the disturbance. DMD shares the frequency isolation properties of SOD and behaves similarly to SOD. It is observed that the three lowest frequency DMD modes reproduce the modal structures well and only a small amount of cross-contamination is observed with the higher-frequency modes.

The above properties of the three modal decomposition techniques are emphasized in the constant amplitude case (Fig. 4). Notice that POD continues to identify three dominant modes, but as POD is an amplitude based decomposition, it can no longer

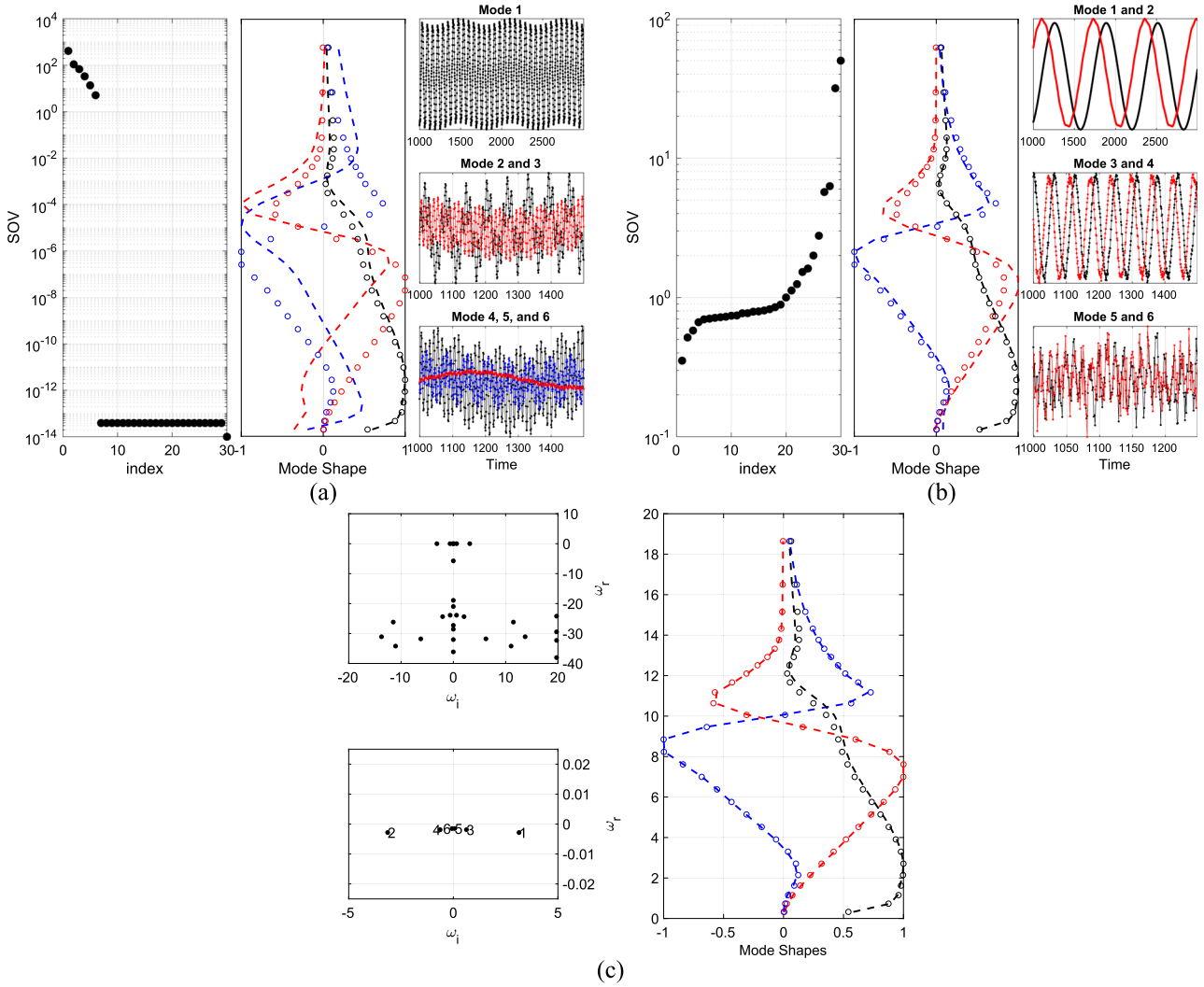

FIG. 5. Propagating oscillations of the variable amplitude. POD (a) and SOD (b): spectra (left), mode shapes (middle), and amplitude coefficients (right). DMD (c): spectra (left) and mode shapes (right). Synthetic data input mode shapes are shown with open circles and decomposition mode shapes are shown with dashed lines. Mode shape are plotted against the y-axis nondimensionalized by the boundary layer length scale.

© Author(s) 2020

distinguish the specific disturbance structure. SOD and DMD, on the other hand, are sensitive to the frequency content and continue to identify disturbance structure well, though DMD modes do contain a slightly larger amount of cross-contamination with higher-frequency modes.

A note concerning mode selection should be pointed out. POD and SOD possess the convenient property of optimally decomposing signal variance. This allows one to interpret the relative importance of the identified modes via their singular values. While DMD does possess aspects of optimization, as described above, much of this interpretation is lost when considering the DMD spectra and it can be difficult to identify the relevance of the individual modes.

2. Propagating Oscillation: Complex(ϕ), Imaginary(λ)

Modal decomposition of the "propagating" synthetic dataset can be seen in Fig. 5, for the variable amplitude disturbance case and in Fig. 6, for the constant amplitude disturbance case. All three decompositions now identify 6 dominant mode shapes. As conjectured above, each physical mode is now associated with a pair of decomposed modes. A pair of modes is required to account for the phase propagation of the physical disturbances. This is particularly clear when considering the amplitude coefficients of the SOD decomposition or the complex conjugate pairs in the DMD spectrum. POD continues to represent the physical signal with an optimal number of statistical modes,

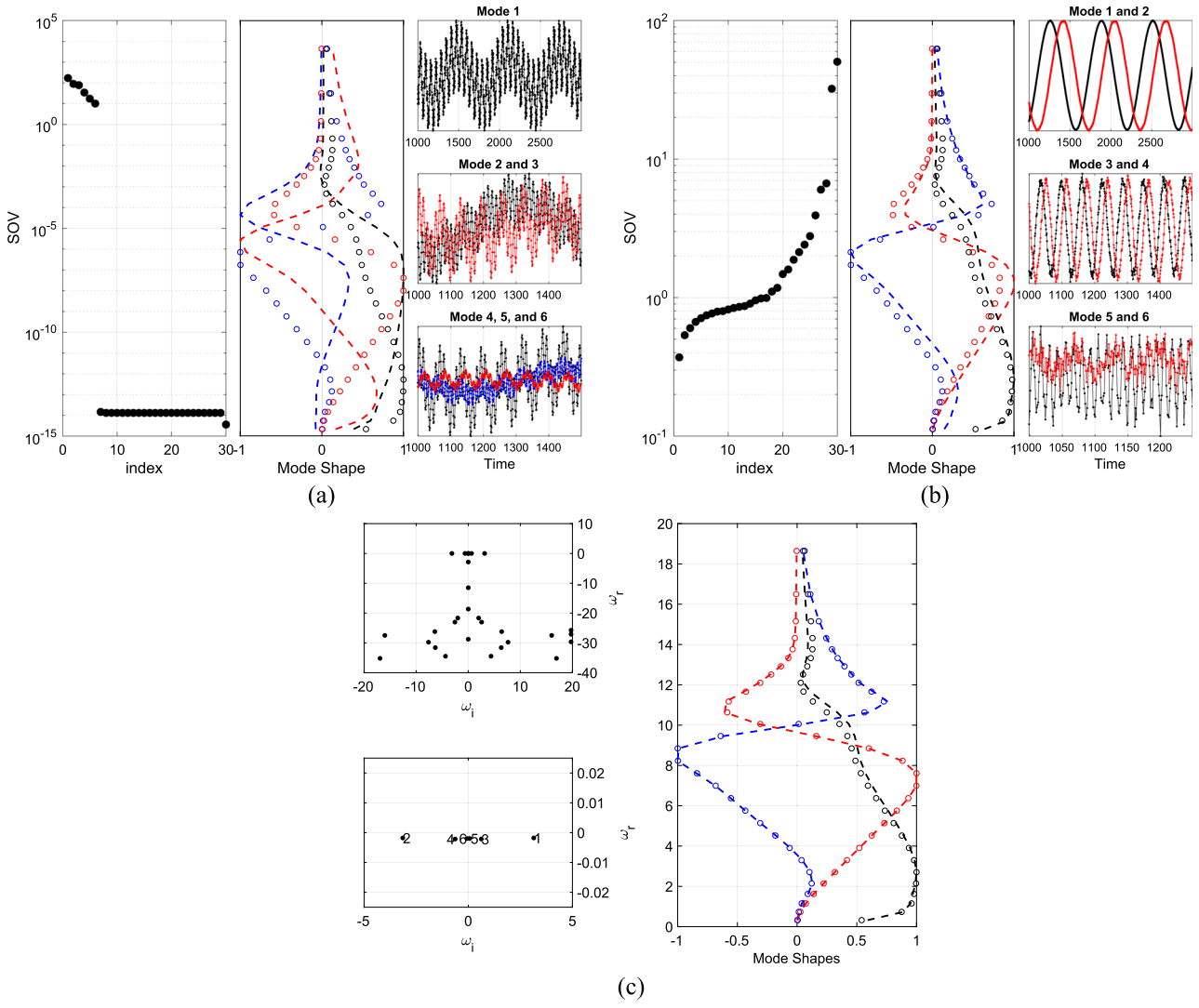

FIG. 6. Propagating oscillations of the constant amplitude. POD (a) and SOD (b): spectra (left), mode shapes (middle), and amplitude coefficients (right). DMD (c): spectra (left) and mode shapes (right). Synthetic data input mode shapes are shown with open circles and decomposition mode shapes are shown with dashed lines. Mode shapes are plotted against the y-axis nondimensionalized by the boundary layer length scale.

© Author(s) 2020

but is unable to isolate individual physical modes. As SOD sorts modes based on both the amplitude and the time scale, groupings of singular values identify disturbances operating on similar time scales and thus, disturbance pairs are straightforward to identify. Note that both SOD and DMD continue to successfully isolate the physical mode structure of the input disturbances.

3. General: Complex(ϕ), Complex(λ)

Modal decomposition of the "general" synthetic dataset can be seen in Fig. 7, for the variable amplitude disturbance case, and in Fig. 8, for the constant amplitude disturbance case. All the general properties of the above studies persist in this case. POD continues to identify statistically optimal modes, but lacks the ability to isolate the physical input disturbances. Both SOD and DMD continue to successfully isolate the physical mode structure of the input disturbances. It is interesting to note that SOD is able to unambiguously identify not only the physical structure of propagating disturbances, but also capture the exponential growth of the disturbance via the amplitude coefficient. While DMD also identifies the physical structure of propagating disturbances and there is indication of exponential growth behavior, there remains ambiguity concerning the actual exponential growth rates.

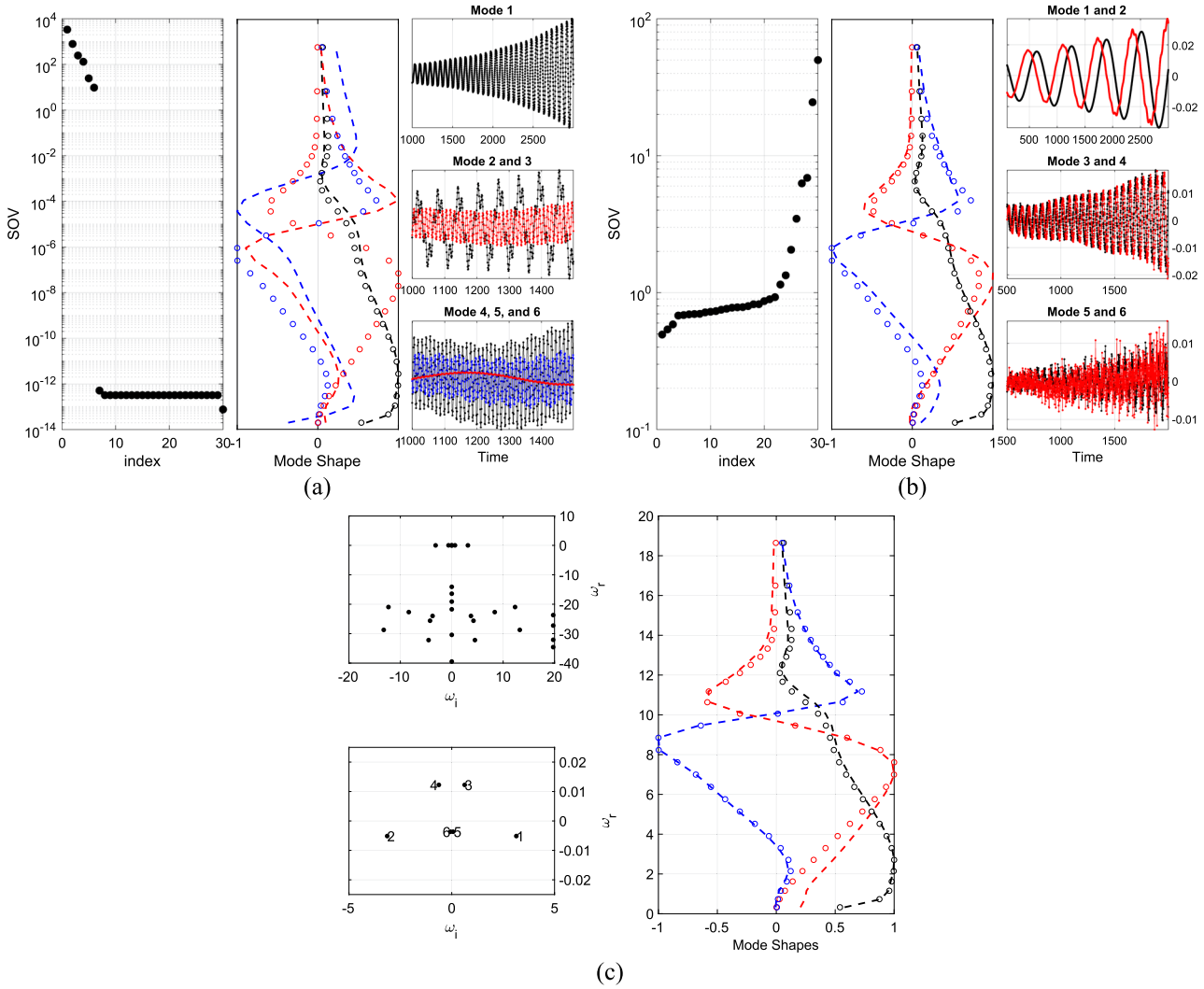

FIG. 7. Exponentially growing and propagating oscillations of the variable amplitude. POD (a) and SOD (b): spectra (left), mode shapes (middle), and amplitude coefficients (right). DMD (c): spectra (left) and mode shapes (right). Synthetic data input mode shapes are shown with open circles and decomposition mode shapes are shown with dashed lines. Mode shapes are plotted against the y-axis nondimensionalized by the boundary layer length scale.

© Author(s) 2020

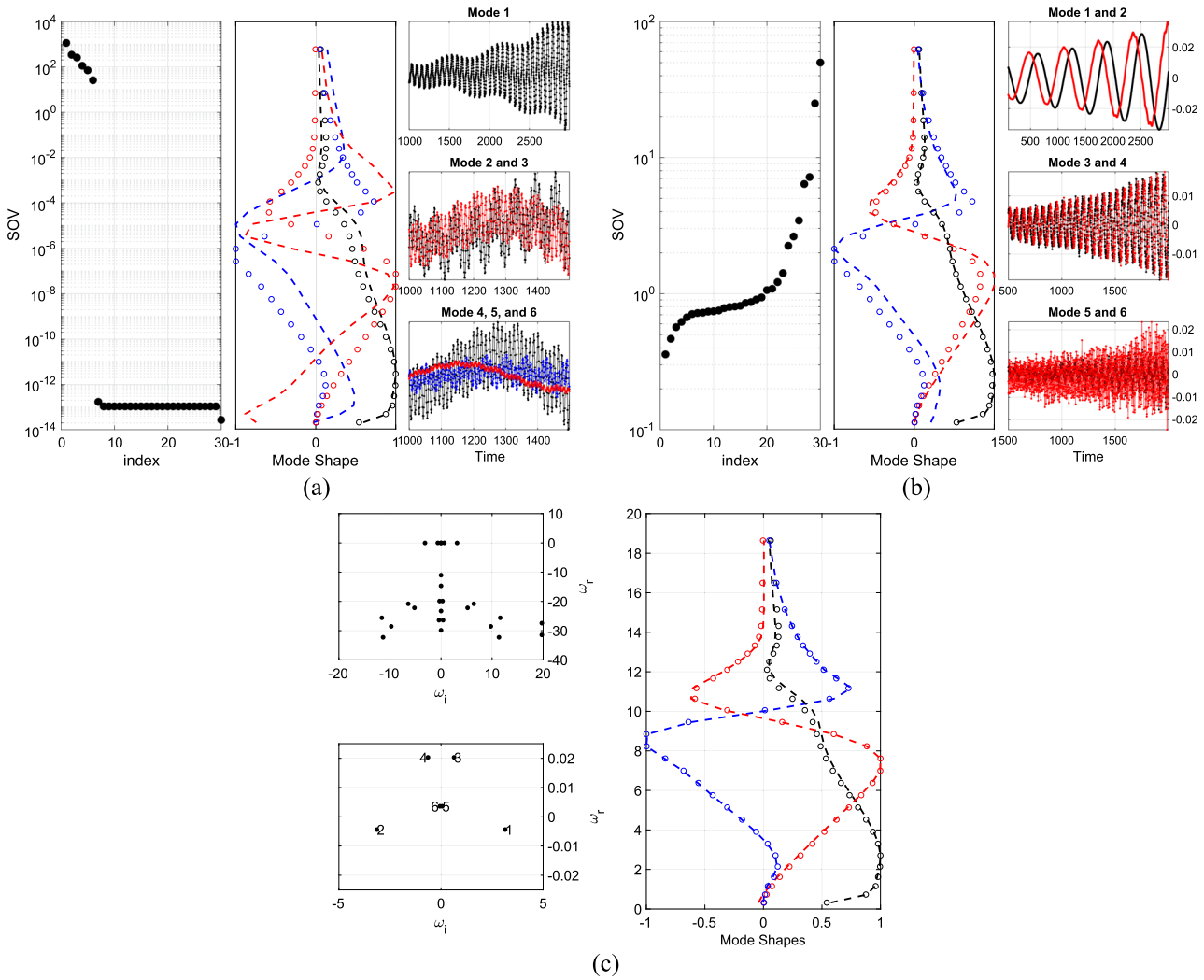

FIG. 8. Exponentially growing and propagating oscillations of the constant amplitude. POD (a) and SOD (b): spectra (left), mode shapes (middle), and amplitude coefficients (right). DMD (c): spectra (left) and mode shapes (right). Synthetic data input mode shapes are shown with open circles and decomposition mode shapes are shown with dashed lines. Mode shape are plotted against the y-axis nondimensionalized by the boundary layer length scale.

VI. CONCLUSION

Here, we have provided a common interpretation of four powerful modal decomposition techniques, which helps unify our understanding of POD, SOD, S-VD, and DMD. Each method can be formulated (at least in part) as a constrained maximization problem, which provides insight into the physical nature of each decomposition. POD considers those modes which maximize amplitude variance of projection, while keeping modes orthogonal. SOD considers those modes which maximize amplitude variance projection, while at the same time keeping these projections as smooth in time as possible. S-VD is a variant of SOD, which allows for the identification of complex vibration modes. DMD also shares this complex mode identification property by the decomposition of the linear evolution operator and can be interpreted as identifying modes that maximize their modal projection onto the time-shifted data matrix while minimizing their projection onto the covariance matrix of the data and time-shifted data for the case of pure exponential growth. However, for the case of pure oscillation, DMD can be interpreted as identifying modes that maximize their modal projection onto the time-shifted data matrix while minimizing their projection onto the original data matrix. The various properties of POD, SOD, and DMD are illustrated by consideration of synthetic hypersonic boundary layer stability data for purely oscillating, propagating, and exponentially growing disturbances.

ACKNOWLEDGMENTS

The authors are thankful to the National Academies of Sciences, Engineering and Medicine Gulf Research Program for

© Author(s) 2020

supporting this research through the award "Taking the Pulse of the West Florida Shelf at a Hypothesized Loop Current Control Point." Dr. Chelidze was supported by the National Science Foundation under Grant No. 1100031.

REFERENCES

[1]G. Berkooz, P. Holmes, and J. L. Lumley, "The proper orthogonal decomposition in the analysis of turbulent flows," Annu. Rev. Fluid Mech. **25**, 539–575 (1993).
[2]A. Chatterjee, "An introduction to the proper orthogonal decomposition," Curr. Sci. **78**, 808–817 (2000).
[3]D. Chelidze and W. Zhou, "Smooth orthogonal decomposition-based vibration mode identification," J. Sound Vib. **292**, 461–473 (2006).
[4]U. Farooq and B. F. Feeny, "An experimental investigation of state-variable modal decomposition for modal analysis," J. Vib. Acoust. **134**(2), 021017 (2011).
[5]B. F. Feeny and U. Farooq, "A nonsymmetric state-variable decomposition for modal analysis," J. Sound Vib. **310**(4-5), 792–800 (2008).
[6]P. J. Schmid, "Dynamic mode decomposition of numerical and experimental data," J. Fluid Mech. **656**, 5–28 (2010).
[7]D. Chelidze and J. P. Cusumano, "Phase space warping: Nonlinear time-series analysis for slowly drifting systems," Philos. Trans. R. Soc., A **364**, 2495–2513 (2006).
[8]D. Chelidze and M. Liu, "Reconstructing slow-time dynamics from fast-time measurements," Philos. Trans. R. Soc., A **366**, 729–745 (2008).
[9]D. Chelidze, "Smooth local subspace projection for nonlinear noise reduction," Chaos **24**, 013121 (2014).
[10]D. B. Segala, D. H. Gates, J. B. Dingwell, and D. Chelidze, "Nonlinear smooth orthogonal decomposition of kinematic features of sawing reconstructions muscle fatigue evolution as indicated by electromyography," J. Biomech. Eng. **133**, 031009 (2011).
[11]J. J. Kuehl, S. F. DiMarco, L. J. Spencer, and N. L. Guinasso, Jr., "Application of the smooth orthogonal decomposition to oceanographic data sets," Geophys. Res. Lett. **41**, 3966, https://doi.org/10.1002/2014GL060237 (2014).
[12]P. J. Schmid, L. Li, M. P. Juniper, and O. Pust, "Applications of the dynamic mode decomposition," Theor. Comput. Fluid Dyn. **25**(1), 249–259 (2010).
[13]P. J. Schmid, "Application of the dynamic mode decomposition to experimental data," Exp. Fluids **50**, 1123–1130 (2011).
[14]J. N. Kutz, S. L. Brunton, B. W. Brunton, and J. L. Proctor, *Dynamic Mode Decomposition: Data-Driven Modeling of Complex Systems* (SIAM, 2016).
[15]A. Chatterjee, J. P. Cusumano, and D. Chelidze, "Optimal tracking of parameter drift in a chaotic system: Experiment and theory," J. Sound Vib. **250**(5), 877–901 (2002).
[16]B. C. Chynoweth, C. Hader, A. Batista, T. J. Juliano, J. Kuehl, B. M. Wheaton, H. F. Fasel, and S. P. Schneider, "A history and progress of research on boundary-layer transition on a Mach 6 flared cone," AIAA Paper 2018-0060, 2018.
[17]B. C. Chynoweth, S. P. Schneider, C. Hader, H. Fasel, A. Batista, J. Kuehl, T. J. Juliano, and B. M. Wheaton, "History and progress of boundary-layer transition on a Mach-6 flared cone," J. Spacecr. Rockets **56**(2), 333–346 (2019).
[18]A. Fedorov, "Transition and stability of high-speed boundary layers," Annu. Rev. Fluid Mech. **43**, 79–95 (2011).
[19]J. Kuehl, "Thermoacoustic interpretation of second-mode instability," AIAA J. **56**, 3585 (2018).
[20]L. M. Mack, "Boundary layer linear stability theory," AGARD Report No. 709, Special course on stability and transition of laminar flow, 1984, pp. 3.1–3.81.
[21]K. M. Casper, S. J. Beresh, and S. P. Schneider, "Pressure fluctuations beneath instability wavepackets and turbulent spots in a hypersonic boundary layer," J. Fluid Mech. **756**, 1058–1091 (2014).
[22]C. Hader and H. Fasel, "Three-dimensional wave packet in a Mach 6 boundary layer on a flared cone," J. Fluid Mech. **885**, R3 (2020).
[23]J. Kuehl, "Discrete and finite bandwidth frequency distributions in nonlinear stability applications," Phys. Fluids **29**(2), 024101 (2017).
[24]A. Batista and J. Kuehl, "A mechanism for spectral broadening and implications for saturation amplitude estimates," AIAA Paper 2017-3635, 2017.
[25]V. C. B. Sousa, A. Batista, J. Kuehl, and C. Scalo, "Nonlinear dynamics of second mode waves on a hypersonic flared cone," AIAA Paper 2018-3852, 2018.
[26]G. V. Candler, H. B. Johnson, I. Nompelis, P. K. Subbareddy, T. W. Drayna, V. Gidzak, and M. D. Barnhardt, "Development of the US3D code for advanced compressible and reacting flow simulations," AIAA Paper 2015-1893, 2015.
[27]I. Nompelis, T. Drayna, and G. Candler, "Development of a hybrid unstructured implicit solver for the simulation of reacting flows over complex geometries," AIAA Paper 2004-2227, 2004.
[28]I. Nompelis, T. Drayna, and G. Candler, "A parallel unstructured implicit solver for hypersonic reacting flow simulation," AIAA Paper 2005-4867, 2005.
[29]J. Kuehl, E. Perez, and H. L. Reed, "JoKHeR: NPSE simulations of hypersonic cross instability," AIAA Paper 2012-0921, 2012.

© Author(s) 2020